

# The Impact of Spectral and Spatial Exciton Distributions on Optical Emission from Thin-Film Weak-Microcavity Organic Light-Emitting Diodes

Ariel Epstein, Nir Tessler, and Pinchas D. Einziger

**Abstract**—We present an analytical model for the optical emission produced by sources located in a thin-film weak-microcavity formation and study the effects of the ensemble spectral and spatial distribution on the device emission properties. However derived for a general stratified media configuration, the formulation results are highly applicable for the study of nanometric organic light-emitting devices. Rigorously developed into closed-form analytical expressions using the device's thin-film weak-microcavity characteristics, they enable clear observation of the underlying physical processes that determine the emission properties of the device, as well as the impact of the exciton ensemble spectral and spatial distributions on these properties. For the sake of simplicity and clarity, we focus on a 2-D canonical configuration excited by impulsive (line) sources. Our results show that the spectral distribution of the ensemble diminishes interference effects originated in the weak microcavity formed between the substrate/air and cathode/active layer interfaces, while the spatial distribution can only impact the slow-varying component of the emission pattern, which is the consequence of the source-image interference near the highly reflecting cathode. For a typical device, the quasi-Lambertian emission pattern reported experimentally is reproduced. It should be pointed out that the incorporation of both rigorous electromagnetic analysis and the source spectral and spatial broadening effects is addressed in our report, to the best of our knowledge, for the first time. This results in a precise model capable of repeating and interpreting experimental and simulated data.

**Index Terms**—Electromagnetic analysis, emission pattern, excitons, microcavity, organic light-emitting diodes.

## I. INTRODUCTION

OPTICAL emission from sources embedded in thin-film stratified media has drawn major interest in the late 1970s, mainly due to the research of fluorescent entities behavior in various environments, which led to the publication of several rigorous electromagnetic analyses [1]–[3]. The problem regains interest in recent years, as the emerging field of organic light-emitting diodes (OLEDs) presents new challenges related to such formations [4]–[6]. The prospects of these devices for novel optoelectronic applications, such as thin and flexible displays, low-cost lasers, and efficient

clean-energy lighting instruments [7]–[12], attract researchers to reveal the physics dominating the device and use these insights for optimizing it for the various applications. The technological effort to design durable and efficient OLEDs with controllable viewing angle [12]–[16] advances hand in hand with the ability to accurately model the emission efficiency and emission pattern of such devices, the underlying physical phenomena, and the dominant factors that determine the device's optical properties [17]–[21].

In this paper, we present a rigorous electromagnetic approach for the OLED radiation problem capable of handling analytically the realistic scenario of an ensemble of excitons, rather than a single coherent emitter. This approach results in closed-form analytical expressions, encapsulating the effects of both the device structure, i.e., layer dimensions and material composition, and the ensemble characteristics, i.e., the spectral and spatial exciton distributions, on important optical parameters. These expressions allow identification of the dominant physical processes as well as the impact of each of them on the device's emission pattern. For the sake of simplicity and clarity, we focus on a 2-D canonical configuration excited by impulsive (line) sources, instead of using the more realistic 3-D dipole model. However, the essence of the problem and the physical phenomena remain the same, and insight gained by the results can, in general, be applied to 3-D devices as well.

## II. THEORY

### A. Formulation

We consider a 2-D device with  $M + N + 2$  layers, with a line source embedded at a certain plane  $z = z'$ , sandwiched between layers  $(-1)$  and  $(+1)$ , as depicted in Fig. 1. The homogeneous layer formed by combining layers  $(-1)$  and  $(+1)$ , containing the line source, is termed the active layer. Each layer is characterized by its permittivity, permeability, and conductivity marked  $\epsilon_n$ ,  $\mu_n$ , and  $\sigma_n$ , respectively, for the  $n$ th layer. Furthermore, the  $n$ th and  $(n + 1)$ th layers are separated by the plane  $z = d_n$  for  $n > 0$  and  $z = d_{n+1}$  for  $n < 0$ , and we define  $d_0 = z'$  and  $d_{N+1} = z$ . Note that  $\epsilon_{-1} = \epsilon_1$ ,  $\mu_{-1} = \mu_1$ , and  $\sigma_{-1} = \sigma_1$ . For the sake of completeness, we treat here both transverse electric and transverse magnetic modes, excited via an electric line source and a magnetic line source (Fig. 1), having current magnitudes of  ${}^e I_0$  and  ${}^m I_0$ , respectively.

Manuscript received January 23, 2010; revised April 7, 2010; accepted April 14, 2010. Date of current version July 23, 2010.

The authors are with the Department of Electrical Engineering, Technion - Israel Institute of Technology, Haifa 32000, Israel (e-mail: arielep@tx.technion.ac.il; nir@ee.technion.ac.il; einziger@ee.technion.ac.il).

Color versions of one or more of the figures in this paper are available online at <http://ieeexplore.ieee.org>.

Digital Object Identifier 10.1109/JQE.2010.2049000

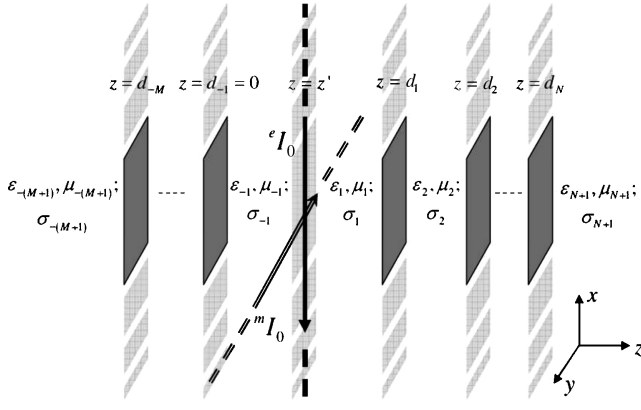


Fig. 1. 2-D configuration for the OLED model. The device consists of  $M + N + 2$  layers, the interfaces of which are planes parallel to the  $\hat{xy}$  plane and the propagation direction is  $\hat{z}$ . The 2-D model excitation is a line source, sandwiched between layers  $(-1)$  and  $(+1)$ , which form together the active layer.

Throughout the paper, we use  $e$  and  $m$  left superscripts or subscripts to denote electric or magnetic cases, respectively. Both sources are assumed to be time harmonic, with time dependence of  $e^{j\omega t}$ . The wave number and wave impedance of the  $n$ th layer are given as  $k_n = \omega \{ \mu_n \epsilon_n [1 - j\sigma_n / (\omega \epsilon_n)] \}^{1/2} = (\omega/c) (\eta_n - j\kappa_n)$  and  $Z_n = (\mu_n / \{ \epsilon_n [1 - j\sigma_n / (\omega \epsilon_n)] \})^{1/2}$ , where  $c$ ,  $n$ , and  $\kappa$  denote the velocity of light in vacuum, refractive index, and extinction coefficient, respectively. To satisfy the radiation condition we require that  $\Im \{ k_n \} \leq 0$ , leading to  $\Im \{ Z_n \} \geq 0$ . Furthermore, we define the 2-D space vector,  $\vec{\rho} = \rho_t \hat{t} + z \hat{z} = (-\rho \sin \theta) \hat{t} + (\rho \cos \theta) \hat{z}$ , where  $\rho_t$  and  $\hat{t}$  are its transverse coordinate magnitude and direction, and  $\theta$  is the angle between the  $z$ -axis and  $\vec{\rho}$ . The transverse coordinate is different for the electric and magnetic cases due to the different symmetry they induce. In the electric line source scenario, there is no change along the  $x$  direction; therefore,  ${}^e[\partial/\partial x] = 0$ ,  ${}^e\rho_t = y$  and  ${}^e\hat{t} = \hat{y}$ . Analogously, for the magnetic line source scenario we have symmetry along the  $y$ -axis; thus,  ${}^m[\partial/\partial y] = 0$ ,  ${}^m\rho_t = x$  and  ${}^m\hat{t} = \hat{x}$ . The source vector in both cases is  $\vec{\rho}' = z' \hat{z}$ .

### B. Spatial and Spectral Distributions

Given the impulse response of the device, or Green's function,  $\mathfrak{G}(\vec{\rho}, \vec{\rho}'; t - t')$ , to a line source excitation at a time  $t'$  and a position  $\vec{\rho}'$ , measured at the observation point  $\vec{\rho}$  at a time  $t$ , the response to an ensemble of sources, with arbitrary temporal and spatial distributions,  $\mathfrak{p}(t')$  and  $f(z')$ , is given by the convolution operator

$$\mathfrak{G}_{ens}(\vec{\rho}, t) = \int dz' f(z') \int dt' \mathfrak{p}(t') \mathfrak{G}(\vec{\rho}, \vec{\rho}'; t - t'). \quad (1)$$

We use the temporal Fourier transform in order to reformat (1) into

$$G_{ens}(\vec{\rho}, \omega) = \int dz' f(z') p(\omega) G(\vec{\rho}, \vec{\rho}'; \omega) \quad (2)$$

where the relation between  $p$  and  $\mathfrak{p}$  (or  $G$  and  $\mathfrak{G}$ ) is given through the Fourier transform, i.e.,  $p(\omega) = \int \mathfrak{p}(t) e^{j\omega t} dt$  and

$\mathfrak{p}(t) = \frac{1}{2\pi} \int p(\omega) e^{-j\omega t} d\omega$ . The spectral distribution of the sources,  $p(\omega)$ , is related to the density of radiatively decaying states, thus resembling photoluminescence spectra [22]. The latter can be usually approximated by a Gaussian [7], [23], [24] and we define, generally

$$p(\omega) = \frac{1}{\Delta\omega\sqrt{2\pi}} \exp \left\{ -\frac{(\omega - \omega_0)^2}{2\Delta\omega^2} \right\} \quad (3)$$

where  $\omega_0$  is the central angular frequency of the ensemble,  $\Delta\omega$  is the distribution spectral width, and  $\int p(\omega) d\omega = 1$ . When several molecular levels contribute to the emission, the photoluminescence is more accurately modeled by a sum of such Gaussians [11], [25], and the formulation can be generalized accordingly. The spatial distribution of sources, being proportional to the variation of the recombination rate along the active layer, can be derived from the solution of the transport equations in the device. In most cases, this solution produces a distribution function in the form of two exponentials, decaying from their common maximum within the active layer toward the cathode and anode [26]–[29]; thus, we define

$$f(z') = \frac{1}{F} \exp \left\{ -\frac{|z' - z'_0|}{W_{\text{sign}\{z' - z'_0\}}} \right\} \quad (4)$$

where  $W_{\pm 1}$  is the exponential decay width toward the cathode  $(-1)$  and anode  $(+1)$ ,  $z'_0$  is the distribution peak location, and  $F$  is a normalization constant assuring that the total probability of sources to be found in the active layer is 1, or,  $\int_{d_{-1}}^{d_1} f(z') dz' = 1$ . Once again, in the more peculiar forms of spatial distributions [30], the model can be readily augmented to include a sum of arbitrary exponentials as the distribution function.

### C. Power Relations

Naturally, the Green function of the device is the electric field,  $\vec{E}(\vec{\rho}, \vec{\rho}'; \omega)$ , or magnetic field,  $\vec{H}(\vec{\rho}, \vec{\rho}'; \omega)$ , induced by the source. However, the physical parameter of interest is the radiated power density averaged over time. The relation between these two defines the emission pattern of the device, given some spectral and spatial distributions

$$S_\rho(\theta) = \int_{d_{-1}}^{d_1} dz' f(z') \cdot \int_{-\infty}^{\infty} d\omega p(\omega) \frac{1}{2} \vec{E}(\vec{\rho}, \vec{\rho}'; \omega) \times [\vec{H}(\vec{\rho}, \vec{\rho}'; \omega)]^* \cdot \hat{\rho} \Big|_{\rho \rightarrow \infty} \quad (5)$$

where we consider the sources to be spatially incoherent [31]. The symmetry of the problem allows us to express the electric and magnetic fields by their transverse components alone. These components are related to the Green function via

$$\begin{aligned} E_x(\vec{\rho}, \vec{\rho}'; \omega) &= jkZJ_s G(\vec{\rho}, \vec{\rho}'; \omega) - M_s \frac{\partial G(\vec{\rho}, \vec{\rho}'; \omega)}{\partial z} \\ H_y(\vec{\rho}, \vec{\rho}'; \omega) &= -J_s \frac{\partial G(\vec{\rho}, \vec{\rho}'; \omega)}{\partial z} + jkYM_s G(\vec{\rho}, \vec{\rho}'; \omega) \end{aligned} \quad (6)$$

where  ${}^e J_s = {}^e I_0$ ,  ${}^m M_s = {}^m I_0$ , and  ${}^m J_s = {}^e M_s = 0$  [32]. The Green function can be expressed via the following spectral integral:

$$G(\vec{\rho}, \vec{\rho}'; \omega) = \frac{1}{2\pi} \int_{-\infty}^{\infty} g(z, z'; \omega) \cdot e^{j\vec{k}_t \cdot \vec{\rho}} dk_t \quad (7)$$

where  $g(z, z'; \omega)$  and  $\vec{k}_t = k_t \hat{t}$  denote the 1-D Green function and transverse wave-vector, respectively. The wave equation and associated constraints for  $g(z, z'; \omega)$  are outlined in [32]–[34]. Expanding the work by Einziger *et al.* [34] we express the Green function in the various layers using recursive relations. For  $z > z'$ , or  $n > 0$

$$g_n(z, z'; \omega) = \frac{e^{j\beta_n z'}}{2j\beta_n} \cdot \frac{1 - \widehat{R}_{-1}(k_t) e^{-2j\beta_n z'}}{1 - R_1(k_t) \widehat{R}_{-1}(k_t)} \left[ \prod_{p=2}^n T_p(k_t) \right] \left[ e^{-j\beta_n z} - R_n(k_t) e^{j\beta_n z} \right] \quad (8)$$

where  $g_n(z, z'; \omega)$  specifies  $g(z, z'; \omega)$  at the  $n$ th layer,  $\beta_n = \sqrt{k_n^2 - k_t^2}$  is the wave number in the propagation direction  $\hat{z}$ , and  $R_n(k_t)$  and  $T_n(k_t)$  are the total reflection and total transmission coefficients, respectively, in the forward direction, i.e., for  $n > 0$ . These coefficients are recursively defined via

$$R_n(k_t) = \left\{ \Gamma_n(k_t) + \frac{[1 - \Gamma_n^2(k_t)] R_{n+1}(k_t) e^{2j\beta_n d_n}}{1 + \Gamma_n(k_t) R_{n+1}(k_t) e^{2j\beta_n d_n}} \right\} e^{-2j\beta_n d_n}$$

$$T_n(k_t) = \frac{[1 + \Gamma_{n-1}(k_t)] e^{j(\beta_n - \beta_{n-1}) d_{n-1}}}{1 + \Gamma_{n-1}(k_t) R_n(k_t) e^{2j\beta_n d_{n-1}}} \quad (9)$$

where  $\Gamma_n(k_t)$  is the forward local reflection coefficient of the  $n$ th interface,  $n > 0$ , given by the Fresnel formula,  $\Gamma_n = (1 - \gamma_n) / (1 + \gamma_n)$ , where we used the definition of the generalized impedance ratio,  ${}^e_m \gamma_n = (Z_{n+1} / Z_n)^{\pm 1} (k_{n+1} / k_n) (\beta_n / \beta_{n+1})$ . The analogous expressions for the reflection and transmission coefficients in the reversed direction,  $\widehat{R}_n(k_t)$ ,  $\widehat{T}_n(k_t)$ , etc., for  $n < 0$ , can be readily derived in a similar manner [35], using the transformations  $(n - 1) \leftrightarrow (n + 1)$  and  $j \leftrightarrow (-j)$ . The recursion stop conditions are  $R_{N+1} = \widehat{R}_{-(M+1)} = 0$ . Substituting (6)–(8) into (5), and taking only the saddle point contribution to the plane wave spectral integral into account [33] we arrive at the following expression for the emission pattern:

$$S_\rho(\theta) \sim P_{N+1} \int_{d_{-1}}^{d_1} dz' f(z')$$

$$\int_{-\infty}^{\infty} d\omega p(\omega) \left| \frac{2j\beta_{N+1} g_{N+1}(z, z'; \omega)}{\sqrt{\pi\rho}} \right|_{k_t = k_{N+1} \sin \theta}^2 \quad (10)$$

where  ${}^e P_n = k_n Z_n |{}^e I_0|^2 / 16$  and  ${}^m P_n = k_n Y_n |{}^m I_0|^2 / 16$  denote the radiation power of electric and magnetic line sources in an unbounded homogeneous medium of the  $n$ th layer material, respectively. Following previous work [36], we express the 1-D Green function in the observation region,  $n = N + 1$ , for  $N, M \geq 1$ , as a sum of multiple reflections between the layers'

boundaries

$$g_{N+1}(z, z'; \omega) = \frac{\prod_{n=1}^{N+1} e^{-j\beta_n(d_n - d_{n-1})} \prod_{n=2}^{N+1} [1 + \Gamma_{n-1}(k_t)]}{2j\beta_{N+1}}$$

$$\cdot \sum_{l'=0}^1 \sum_{l_1=-1}^{\infty} e^{-2j\beta_1[l'z' + (l_1+1)d_1 - (\hat{l}_{-1}+1)d_{-1}] + j'l'\pi}$$

$$\cdot \sum_{s_1=0}^{l_1+1} \sum_{p_1=0}^{l_{N-1}+1} \cdots \sum_{s_{N-1}=0}^{l_{N-1}+1} \sum_{p_{N-1}=0}^{\infty} K(1, N, l_q, s_q, p_q)$$

$$\cdot \sum_{\hat{s}_{-1}=0}^{\hat{l}_{-1}+1} \sum_{\hat{p}_{-1}=0}^{\hat{l}_{-(M-1)}+1} \cdots \sum_{\hat{s}_{-(M-1)}=0}^{\hat{l}_{-(M-1)}+1} \sum_{\hat{p}_{-(M-1)}=0}^{\infty} \widehat{K}(-M, -1, \hat{l}_q, \hat{s}_q, \hat{p}_q)$$

$$\cdot \prod_{n=2}^N \left\{ \sum_{\tilde{l}_n=-1}^{\infty} [-\Gamma_{n-1}(k_t)]^{\tilde{l}_n+1} e^{-2j(\tilde{l}_n+1)\beta_n(d_n - d_{n-1})} \right.$$

$$\left. \sum_{\tilde{s}_n=0}^{\tilde{l}_n+1} \sum_{\tilde{p}_n=0}^{\tilde{l}_{N-1}+1} \cdots \sum_{\tilde{s}_{N-1}=0}^{\tilde{l}_{N-1}+1} \sum_{\tilde{p}_{N-1}=0}^{\infty} K(n, N, \tilde{l}_q^n, \tilde{s}_q^n, \tilde{p}_q^n) \right\} \quad (11)$$

where we must consider all the possible combinations for reflections a plane wave encounters along its propagation within the device; thus, we define

$$K(n_1, n_2, l_q, s_q, p_q) = [\Gamma_{n_2}(k_t)]^{\tilde{l}_{n_2}+1}$$

$$\prod_{q=n_1}^{n_2-1} \binom{l_q+1}{s_q} \binom{l_q+1}{p_q} e^{-2j(l_{q+1}+1)\beta_{q+1}(d_{q+1} - d_q)}$$

$$[-\Gamma_q(k_t)]^{p_q} [1 - \Gamma_q^2(k_t)]^{l_q - s_q + 1} [\Gamma_q(k_t)]^{s_q}$$

$$\quad (12)$$

and  $\widehat{K}$  is given by transforming (12) using  $(q - 1) \leftrightarrow (q + 1)$  and  $j \leftrightarrow (-j)$ ; moreover  $\hat{l}_n = \sum_{k=1}^{n-1} (p_k - s_k) + l_1$ ,  $\hat{l}_n = \sum_{k=n+1}^{-1} (\hat{p}_k - \hat{s}_k) + \hat{l}_{-1}$ ,  $\hat{l}_{-1} = l' + l_1$  and  $\tilde{l}_q^n = \sum_{k=n}^{q-1} (\tilde{p}_k^n - \tilde{s}_k^n) + \tilde{l}_n^n$ .

#### D. Spectral Distribution Effect

Assuming that in the relevant spectral interval of (3),  $\omega_0 \pm \Delta\omega$ , the optical parameters of the media, i.e.,  $n_n$  and  $\kappa_n$ , do not vary significantly with  $\omega$ , we get that after the substitution  $k_t = k_{N+1} \sin \theta$  of (10), all  $\beta_n$  are proportional to  $\omega$ , and all  $\Gamma_n$  and  $\widehat{\Gamma}_n$  are independent of the field's angular frequency. Incorporating (11) into (10), the latter can be reformatted as a sum of multiple reflection terms, and the spectral and spatial integrals can be solved, term-by-term. Each term takes the form of a multiple reflection combination, consisting of a reflection coefficient product,  $\alpha_q(\theta)$ , independent of  $\omega$ , and a phase factor,  $e^{-2jk_{N+1}(\omega)l_q(\theta)} = e^{-2j\omega\tau_q(\theta)}$ , accumulating a linear phase relative to the propagation induced by the multiple reflections defined by  $\alpha_q(\theta)$ . The parameters  $l_q(\theta)$  and  $\tau_q(\theta)$  define the optical propagation length and propagation time, respectively, within the device, and are also independent of the angular frequency. The spectral integral for a single term can therefore be solved analytically, leading to

$$\int_{-\infty}^{\infty} d\omega p(\omega) \sum_{q=-\infty}^{\infty} \alpha_q(\theta) e^{-2jk_{N+1}(\omega)l_q(\theta)}$$

$$= \sum_{q=-\infty}^{\infty} \alpha_q(\theta) e^{-2jk_{N+1}(\omega_0)l_q(\theta)} e^{-\frac{1}{2}[2l_q(\theta)/L_c]^2}$$

$$\quad (13)$$

where the coherence length for the ensemble,  $L_c = c/\Delta\omega = \lambda^2/(2\pi\Delta\lambda)$ , is defined as the optical length in air until which two photons generated by the ensemble at the same moment with the same initial phase can be still considered coherent [37], i.e., their frequency difference does not induce a significant phase difference upon propagation distance up to  $L_c$ . The use of the term ‘‘coherence length’’ in this context does not imply a consistent emission from different excitons (their emission was already shown to be occurring in random times and locations [31]) as one might infer from this phrase. Instead, it indicates the ability of coherent interference between a source and its reflections to be pronounced in the device response after integration over all of the ensemble contributions; as shown, this ability is strongly dependent on the exciton spectral distribution width. This is a very important result, as it suggests that multiple reflection combinations that induce large optical propagation distances with respect to the coherence length,  $L_c \ll 2l_q(\theta)$ , can be neglected from the summation of (11), when the ensemble total response is considered.

### E. Spatial Distribution Effect

Solving the spatial integral involves only the first two factors in (8), as all other factors are independent of the source location,  $z'$ . Referring to the relevant form of these factors in (10),  $\left| e^{j\beta_1(z'-d_{-1})} - \widehat{R}_{-1} e^{-j\beta_1(z'-d_{-1})} \right|^2$ , we arrive at

$$\begin{aligned} & \int_{d_{-1}}^{d_1} dz' f(z') \sum_{r=-1,0,+1} \alpha_r(\theta) e^{-2j[(z'-d_{-1})/l_r(\theta,\omega)]} \\ &= \sum_{r=-1,0,+1} \alpha_r(\theta) e^{-2j[(z'_0-d_{-1})/l_r(\theta,\omega)]} \\ & \quad \frac{\sum_{u=-1,+1} \frac{uW_u}{u+2jW_u/l_r} \left[ 1 - e^{-2j(d_u-z'_0)/l_r} e^{-|d_u-z'_0|/W_u} \right]}{\sum_{u=-1,+1} W_u \left[ 1 - e^{-|d_u-z'_0|/W_u} \right]} \quad (14) \\ &= \sum_{r=-1,0,+1} \alpha_r(\theta) e^{-2j[(z'_0-d_{-1})/l_r(\theta,\omega)]} \frac{F_b(l_r, z'_0)}{F} \end{aligned}$$

where  $l_r(\theta, \omega)$  is the effective wavelength for the  $r$ th term, and  $F_b(l_r, z'_0)/F$  is the spatial broadening factor for the  $r$ th term. It is readily observed that if the spatial widths  $W_{\pm 1}$  are very small with respect to the active layer dimensions, then  $F_b(l_r, z'_0)/F$  approaches 1, and  $f(z')$  takes the form of a delta function, as expected. On the other hand, if the spatial broadening is substantial,  $F_b(l_r, z'_0)/F$  decreases the weight of the  $r$ th term as the spatial widths  $W_{\pm 1}$  increase. This can be inferred from the approximations we present for the symmetric distribution cases, where  $W_1 = W_{-1} = W$ . If the ensemble center is close to the active layer boundaries,  $z'_0 \rightarrow d_{\pm 1}$ , a good approximation is

$$\left. \frac{F_b(l_r, z'_0)}{F} \right|_{z'_0 \rightarrow d_{\pm 1}} \approx \frac{1 \pm j(2W/l_r)}{1 + (2W/l_r)^2} \quad (15)$$

whereas when the excitons are concentrated around the middle of the active layer,  $z'_0 \rightarrow (d_1 - d_{-1})/2 = d/2$ , the spatial

broadening factor is given by

$$\left. \frac{F_b(l_r, z'_0)}{F} \right|_{z'_0 \rightarrow d/2} = \frac{1 + e^{-d/(2W)} [(2W/l_r) \sin(d/l_r) - \cos(d/l_r)]}{[1 + (2W/l_r)^2] [1 - e^{-d/(2W)}]} \quad (16)$$

which is an accurate expression if  $z'_0 = d/2$ . For other values of  $z'_0$ , the spatial broadening factor lies between these two limiting cases.

For exciton ensembles located far from the active layer boundary at  $d_{-1}$ , the phase term  $(z'_0 - d_{-1})\beta_1/k_{N+1}$  becomes comparable with the typical coherence length (typical values will be introduced in Section II-F later on), and the effect of the spectral broadening on the location-dependent terms cannot be totally neglected. In those cases, we must execute the spectral integral as well, leading to

$$\begin{aligned} & \int_{d_{-1}}^{d_1} dz' f(z') \int_{-\infty}^{\infty} d\omega p(\omega) \sum_{r=-1,0,+1} \alpha_r(\theta) e^{-2j[(z'-d_{-1})/l_r(\theta,\omega)]} \\ &= \sum_{r=-1,0,+1} \alpha_r(\theta) e^{-2j[(z'_0-d_{-1})/l_r(\theta,\omega)]} \frac{F_b(l_r, z'_0)}{F} \\ & \quad \exp \left\{ -\frac{1}{2} \left[ \frac{2(z'_0-d_{-1})}{l_r(\theta,\omega)k_{N+1}(\omega)L_c} \right]^2 \right\} \\ &= \sum_{r=-1,0,+1} \alpha_r(\theta) e^{-2j[(z'_0-d_{-1})/l_r(\theta,\omega)]} \frac{\widetilde{F}_b(l_r, z'_0, \omega_0)}{F} \quad (17) \end{aligned}$$

where the Gaussian decay varies much slower with  $z'$  than the spatial distribution factor, and thus can be removed from the integrand for the spatial integration. For typical exciton spatial distributions and coherence lengths the Gaussian factor remains close to unity; however, in some cases, as discussed above, the  $r$ th term in (14) experiences an additional attenuation due to the spectral distribution of the sources, and the corrected spatial broadening factor,  $\widetilde{F}_b(l_r, z'_0, \omega_0)/F$ , must be used.

### F. Closed-Form Solution for Prototype Device

In order to demonstrate the impact of the last two results, i.e., the effect of spectral and spatial source distributions on the optical emission from thin-film weak-microcavity formations, we apply them to a prototype device. A basic configuration of a five-layer bottom emitting (BE)-OLED is selected [7]. The elementary device, specified in Table I and depicted in Fig. 2, corresponds to Fig. 1 (setting  $M = 1$  and  $N = 3$ ) with an electric line source excitation located at  $z' = 20$  nm, radiates typically at  $\lambda \approx 600$  nm [24].

We observe three important typical optical features of such a device. First, it indeed forms a weak-microcavity structure, as the silver/polymer interface is the only significant reflecting boundary with  $|\widehat{\Gamma}_{-1}(k_t \rightarrow 0)| \sim 97\%$  field reflection upon perpendicular incidence; the second most reflecting boundary is the glass/air interface with  $\Gamma_3(k_t \rightarrow 0) \sim 20\%$  field reflection upon perpendicular incidence, increasing up to 100% for larger values of  $k_t$ , the maximum reached when  $k_t = k_4$  (10), i.e., when the angle of incidence upon the glass/air interface equals the critical angle for total internal reflection. Second, the polymer and indium tin oxide (ITO) layer dimensions

TABLE I  
GEOMETRICAL AND ELECTRICAL PROPERTIES OF A PROTOTYPE  
BE-OLED, CORRESPONDING TO FIG. 1 (DATA ARE RETRIEVED FROM  
[20] AND [24])

$n$	Layer Material	$n_n$	$\kappa_n$	$d_n$ [nm]
-2	Silver	0.124	3.73	$-\infty$
-1	MEH-DOO-PPV	1.9	0.01	0
+1	MEH-DOO-PPV	1.9	0.01	200
+2	ITO	1.85	0.0065	300
+3	Glass	1.5	0	$10^6$
+4	Air	1	0	$+\infty$

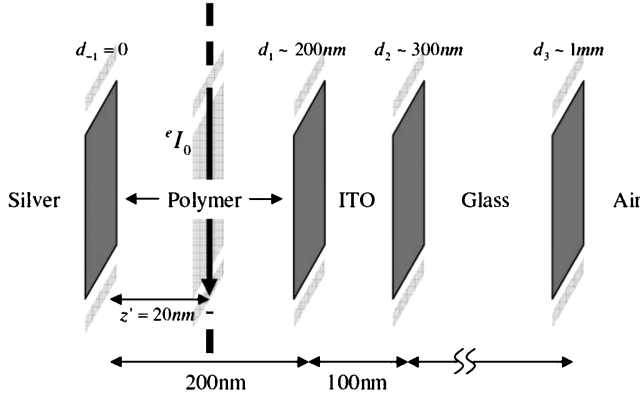


Fig. 2. Physical configuration of the prototype BE-OLED specified in Table I.

are comparable with the emission wavelength in the media, i.e., they are considered thin-film layers, whereas the glass substrate thickness is greater by several orders of magnitude. Third, the typical emission spectral width of these devices [7], [23], [24], [38] is  $\Delta\lambda \sim 50\text{nm} - 75\text{nm}$ , which corresponds to a coherence length of  $L_c \sim 0.764\ \mu\text{m} - 1.145\ \mu\text{m}$ , only slightly larger than the wavelength, but much smaller than the substrate thickness.

The first observation, relating to the weak-microcavity characteristics of the device, implies that only a handful of terms in (11) are significant, as term amplitudes, being proportional to products of reflection coefficients, are much less than unity and decrease dramatically for increasing number of internal reflections. This leads to

$$g_4(z, z'; \omega) \approx \frac{e^{j\beta_1(z'-d_{-1})} \hat{\Gamma}_{-1}(k_t) e^{-j\beta_1(z'-d_{-1})}}{2j\beta_4} \cdot e^{-j\beta_1(d_1-d_{-1})} \prod_{n=2}^4 [1 + \Gamma_{n-1}(k_t)] e^{-j\beta_n(d_n-d_{n-1})} \cdot \sum_{\nu=0}^{v_{\max}} \left\{ \hat{\Gamma}_{-1}(k_t) [\Gamma_2(k_t) + \Gamma_3(k_t) e^{-2j\beta_3(d_3-d_2)}] \right\}^{\nu} \cdot \left\{ e^{-2j\beta_2(d_2-d_1)} e^{-2j\beta_1(d_1-d_{-1})} \right\}^{\nu} \quad (18)$$

where we limit the number of internal reflections,  $\nu$ , by the value of  $v_{\max} = 3$ , which is sufficiently accurate for our case. The second observation, relating to the thin-film characteristics of the device, implies that the effect of the spatial distribution of sources on the emission pattern, according to (14), is limited to the slow-varying component of the emission pattern, as it can only impact the image-source interference term, which

meets the half-wavelength (Bragg) conditions only a few times for these typical layer dimensions and emission wavelengths. The third observation implies that all terms in (11), which involve phase factors due to propagation in the glass layer, effectively vanish according to (13). This is achieved by incorporating (18) into (10), using (13) and the realistic values of the coherence length, implying  $L_c \ll (d_3 - d_{-1})$ . Finally we arrive at

$$S_{\rho}(\theta) \approx \frac{P_4}{\pi\rho} T_{IS}(k_t, z'_0) T_{DR}(k_t) T_{WM}(k_t) \Big|_{k_t=k_4 \sin \theta} \quad (19)$$

where we define the simplified image-source, direct-ray and weak-microcavity transmission factors, respectively, as follows:

$$T_{IS}(k_t, z'_0) = e^{-2\Im\{\beta_1\}(z'_0-d_{-1})} - 2\Re \left\{ \hat{\Gamma}_{-1}(k_t) e^{-2j\Re\{\beta_1\}(z'_0-d_{-1})} \frac{\tilde{F}_b(1/\Re\{\beta_1\}, z'_0, \omega_0)}{F} \right\} + \left| \hat{\Gamma}_{-1}(k_t) \right|^2 e^{2\Im\{\beta_1\}(z'_0-d_{-1})} \quad (20)$$

$$T_{DR}(k_t) = e^{2\Im\{\beta_1\}(d_1-d_{-1})} \cdot \prod_{n=2}^4 |1 + \Gamma_{n-1}(k_t)|^2 e^{2\Im\{\beta_n\}(d_n-d_{n-1})} \quad (21)$$

$$T_{WM}(k_t) = \sum_{\nu=0}^{v_{\max}} \left\{ \left| \hat{\Gamma}_{-1}(k_t) \right|^2 \left| \Gamma_3(k_t) \right|^2 e^{4\Im\{\beta_3\}(d_3-d_2)} e^{4\Im\{\beta_2\}(d_2-d_1)} e^{4\Im\{\beta_1\}(d_1-d_{-1})} \right\}^{\nu} \quad (22)$$

The power relation as formulated in (19), together with the definitions (20)–(22), constitutes a very important result. In its analytical closed form we can readily identify the dominant optical processes in the device, namely, the image-source interference (20), which is strongly dependent on the exciton positions with respect to the cathode; the direct ray contribution (21), which includes the propagation phase accumulation and transmission through layers; and the weak-microcavity effects (22), which consist of multiple reflections between the cathode/polymer and glass/air interfaces. The impact of the spatial and spectral source distributions is mediated by the spatial broadening factor,  $F_b(1/\Re\{\beta_1\}, z'_0)/F$ , multiplying the image-source interference term in (20), and the absence of the weak-microcavity cross-terms from (22), which vanish due to the large substrate dimensions with respect to realistic coherence lengths. This result of the rigorous derivation is capable of reproducing the measured emission patterns as well as evaluating the quality and validity of heuristic approaches, such as semi-infinite glass [20], perturbed glass thickness [22], or ray-optics [17], [18].

### III. RESULTS AND DISCUSSION

#### A. Spectral Distribution Effect

Emission patterns of prototype BE-OLEDs with varying either spectral distribution widths or glass thicknesses are depicted in Figs. 3 and 4, respectively. In both figures the spatial distribution is defined as the delta function,  $f(z') =$

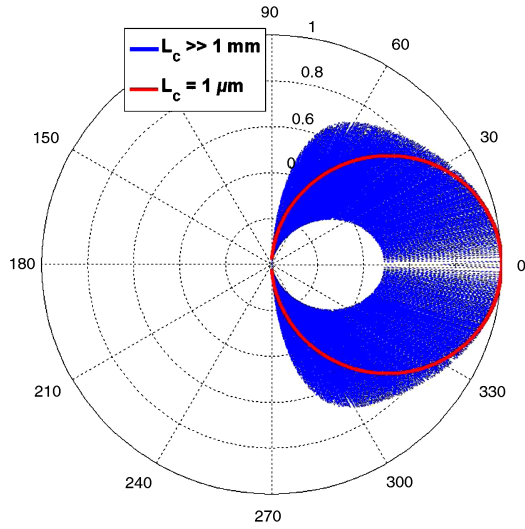


Fig. 3. Effect of exciton spectral distribution width, or coherence length, on the OLED emission pattern, for electric line source excitation at  $z'_0 = 20$  nm, infinitesimal spatial distribution width,  $W_{-1} = W_1 \ll (d_1 - d_{-1})$ ,  $\lambda$  and two coherence length values:  $L_c \gg (d_3 - d_{-1}) \sim 1$  mm (blue-dotted line) and  $L_c = 1 \mu\text{m} \ll (d_3 - d_{-1})$  (red solid line). The former was calculated using (18), while for the latter, (19) was used.

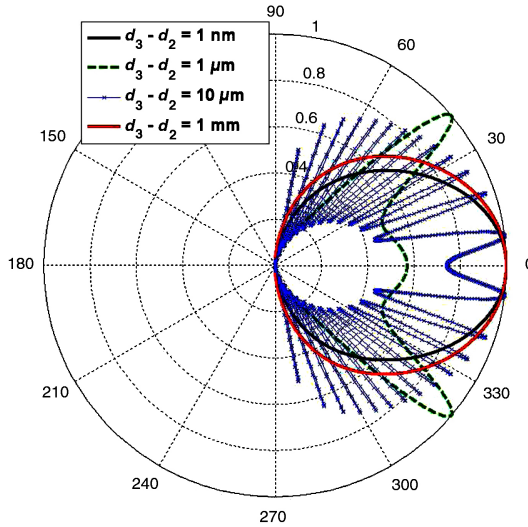


Fig. 4. Effect of glass thickness on the OLED radiation pattern, for electric line source excitation at  $z'_0 = 20$  nm, infinitesimal spatial distribution width,  $W_{-1} = W_1 \ll (d_1 - d_{-1})$ ,  $\lambda$ , large but finite coherence length  $L_c = 150 \mu\text{m}$  and four glass thickness values: 1 nm (black solid line), 1  $\mu\text{m}$  (green-dashed line), 10  $\mu\text{m}$  (blue line with x marker) and 1 mm (red solid line). The patterns were calculated using (18) in conjunction with (13).

$\delta(z' - z'_0)$ ,  $z'_0 = 20$  nm, in order to isolate the effect of the spectral distribution. Fig. 3 presents emission patterns for two values of coherence length, the single coherent source case, calculated using (18), and the realistic  $L_c \sim 1 \mu\text{m}$  case, for which (19) is applicable. As expected, we see that for an infinite coherence length, the weak microcavity induced interference dominates the fast-varying component of the pattern, and multiple maxima and minima appear in the angles for which the Bragg condition is met. In the realistic case of a finite coherence length in the order of  $L_c \sim 1 \mu\text{m}$ , much smaller than the weak-microcavity optical length, the

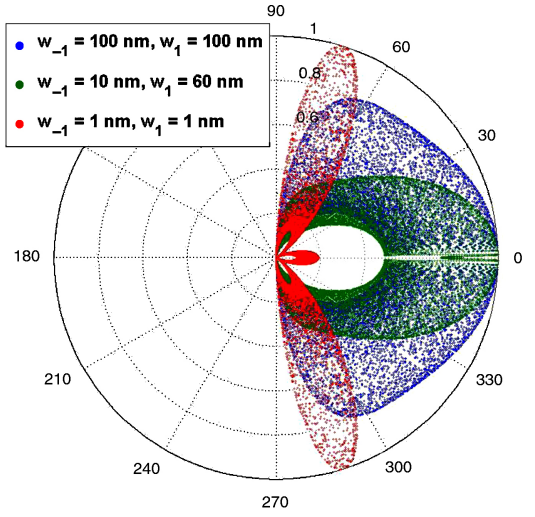


Fig. 5. Effect of exciton spatial distribution widths on the OLED emission pattern, for electric line source excitation at  $z'_0 = 140$  nm, infinite coherence length,  $L_c \gg (d_3 - d_{-1})$ , and three spatial distribution widths:  $W_{-1} = W_1 = 100$  nm (blue circles),  $W_{-1} = 10$  nm,  $W_1 = 60$  nm (green circles), and  $W_{-1} = W_1 = 1$  nm (red circles). The emission patterns were calculated using (18) in conjunction with (14).

fast-varying response vanishes completely, and the reported quasi-Lambertian response is observed.

This effect is further emphasized in Fig. 4, where the coherence length is set to a finite, although unreasonably large for OLEDs, value of  $L_c = 150 \mu\text{m}$ , i.e., a very narrow emission linewidth, which allows some additional observations upon variation of the glass thickness in the range  $d_3 - d_2 = 1$  nm–1 mm. It is readily observed that for device thickness (represented by the dominant glass thickness) much smaller than the coherence length, interference effects are noticeable whereas the reversed situation results in a quasi-Lambertian emission pattern. Furthermore, these observations agree well with experimental measurements taken in the two limits [14], [20]. Note that the two extremes correspond to emission patterns that reflect either the device properties, i.e., thickness-dependent interference according to the half-wavelength condition, or the source characteristics, leading to spectral broadening dominated pattern.

### B. Spatial Distribution Effect

In order to observe the effect of the spatial distribution on the emission pattern we must choose the center of the distribution to be in a location where the image-source interference is significant. Thus, in Figs. 5 and 6 we plot the emission patterns for a source distribution with maximum at  $z'_0 = 140$  nm, and vary the distribution widths from  $W_{-1} = W_1 = 1$  nm to  $W_{-1} = W_1 = 100$  nm. In order to stress the different impacts of the spatial and spectral broadening, Fig. 5 is plotted for the prototype device taking the coherence length to be infinite, whereas the same plots are presented in Fig. 6 with a realistic coherence length of  $L_c = 1 \mu\text{m}$ . As discussed above, for small spatial distribution widths, the distribution function approaches the delta function; therefore, the response for these parameter values in Fig. 5 is the same as for a single coherent source.

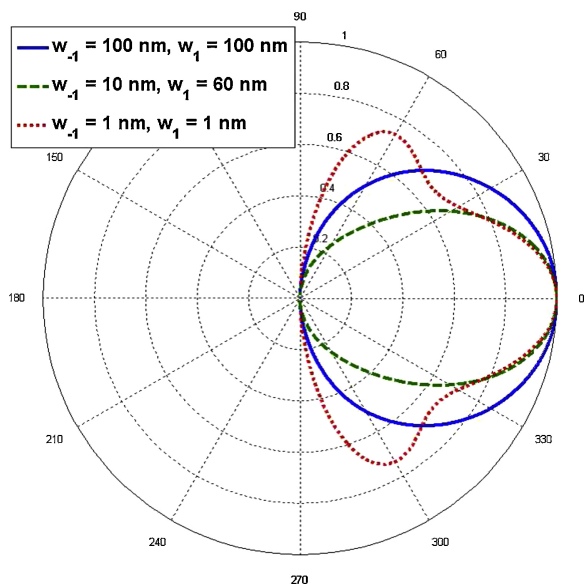


Fig. 6. Effect of exciton spatial distribution widths on the OLED emission pattern, for electric line source excitation at  $z'_0 = 140 \text{ nm}$ , realistic coherence length,  $L_c = 1 \mu\text{m} \ll (d_3 - d_{-1})$ , and three spatial distribution widths:  $W_{-1} = W_1 = 100 \text{ nm}$  (blue solid line),  $W_{-1} = 10 \text{ nm}$ ,  $W_1 = 60 \text{ nm}$  (green-dashed line), and  $W_{-1} = W_1 = 1 \text{ nm}$  (red-dotted line). The emission patterns were calculated using (19).

When the distribution width increases, the original image-source interference pattern disappears, as the interference term is diminished according to (14). Similar attenuation of image-source interference patterns due to exciton spatial distribution broadening can be observed in the results of Savaidis and Stathopoulos [21], where the authors present simulated OLED electroluminescence spectra, which also usually contain extrema on wavelengths that match the Bragg condition.

In addition, it is clear that, as expected, the spatial distribution broadening cannot affect the fast-varying component of the emission pattern, which is related to much larger length scales; therefore, this component is evident when the chosen spectral distribution is narrow enough, as in Fig. 5. However, introduction of spectral broadening of realistic coherence length, as in Fig. 6, averages this fast-varying component, or large-scale interference phenomena. Another feature noticeable in Fig. 6 is that for a very small spatial broadening, e.g.,  $W_{-1} = W_1 = 1 \text{ nm}$ , we may observe some effect of the spectral broadening even on the image-source interference process. The intensity of this effect strongly depends on the relation between the coherence length and the optical distance from the source to its image, as formulated in (17) and discussed therein.

It is worth noting that emission patterns associated with the commonly used aluminum cathode will experience minor shifts in the image-source interference extrema, due to the different metal/polymer reflection coefficient phase. Nevertheless, the formulation results as well as the essence of the physical processes remain the same.

#### IV. CONCLUSION

A complete analysis for the optical emission from 2-D thin-film weak-microcavity formations, incorporating spatial

and spectral source distributions effects, has been presented and verified through numerical simulations for a basic BE-OLED configuration. The results imply that realistic values of spectral and spatial distribution widths can explain the transformation between emission patterns typical to a single coherent source and the experimentally observed quasi-Lambertian patterns. Moreover, the closed-form expressions derived for a prototype BE-OLED reveal that the exciton ensemble spectral broadening is responsible for the vanishing of the fast-varying component of the emission pattern, related to the weak-microcavity interference effects, whereas the effect of the spatial distribution is limited to the slow-varying component of the emission pattern, resulting from the image-source interference induced by the presence of the metallic cathode. These resultant analytical expressions preserve the physical intuition of the device optics and allow for an efficient implementation and design. Furthermore, as demonstrated for the prototype device, they establish a clear and simple relation between the device structure, the ensemble statistics, and the emission pattern.

#### REFERENCES

- [1] R. R. Chance, A. Prock, and R. Silbey, "Molecular fluorescence and energy transfer near interfaces," *Adv. Chem. Phys.*, vol. 37, pp. 1–65, 1978.
- [2] W. Lukosz, "Theory of optical-environment-dependent spontaneous-emission rates for emitters in thin layers," *Phys. Rev. B*, vol. 22, no. 6, pp. 3030–3038, 1980.
- [3] W. Lukosz, "Light emission by multipole sources in thin layers. I: Radiation patterns of electric and magnetic dipoles," *J. Opt. Soc. Am.*, vol. 71, no. 6, pp. 744–754, 1981.
- [4] H. Becker, S. E. Burns, and R. H. Friend, "Effect of metal films on the photoluminescence and electroluminescence of conjugated polymers," *Phys. Rev. B*, vol. 56, no. 4, pp. 1893–1905, Jul. 1997.
- [5] N. Danz, J. Heber, A. Bräuer, and R. Kowarschik, "Fluorescence lifetimes of molecular dye ensembles near interfaces," *Phys. Rev. A*, vol. 66, no. 6, p. 063809, Dec. 2002.
- [6] R. M. Amos and W. L. Barnes, "Modification of the spontaneous emission rate of  $eu3+$  ions close to a thin metal mirror," *Phys. Rev. B*, vol. 55, no. 11, pp. 7249–7254, Mar. 1997.
- [7] R. H. Friend, R. W. Gymer, A. B. Holmes, J. H. Burroughes, R. N. Marks, C. Taliani, D. D. C. Bradley, D. A. D. Santos, J. L. Bredas, M. Logdlund, and W. R. Salaneck, "Electroluminescence in conjugated polymers," *Nature*, vol. 397, no. 6715, pp. 121–128, 1999.
- [8] N. Tessler, G. J. Denton, and R. H. Friend, "Lasing from conjugated-polymer microcavities," *Nature*, vol. 382, no. 6593, pp. 695–697, 1996.
- [9] H. Sirringhaus, N. Tessler, and R. H. Friend, "Integrated optoelectronic devices based on conjugated polymers," *Science*, vol. 280, no. 5370, pp. 1741–1744, 1998.
- [10] V. G. Kozlov, G. Parthasarathy, P. E. Burrows, V. B. Khalfin, J. Wang, S. Y. Chou, and S. R. Forrest, "Structures for organic diode lasers and optical properties of organic semiconductors under intense optical and electrical excitations," *IEEE J. Quantum Elect.*, vol. 36, no. 1, pp. 18–26, Jan. 2000.
- [11] N. Tessler, V. Medvedev, M. Kazes, S. Kan, and U. Banin, "Efficient near-infrared polymer nanocrystal light-emitting diodes," *Science*, vol. 295, no. 5559, pp. 1506–1508, 2002.
- [12] D. Reineke, F. Lindner, G. Schwartz, N. Seidler, K. Walzer, B. Lüssem, and K. Leo, "White organic light-emitting diodes with fluorescent tube efficiency," *Nature*, vol. 459, no. 7244, pp. 234–238, 2009.
- [13] T. Nakamura, N. Tsutsumi, N. Juni, and H. Fujii, "Thin-film waveguiding mode light extraction in organic electroluminescent device using high refractive index substrate," *J. Appl. Phys.*, vol. 97, no. 5, p. 054505, 2005.
- [14] F. Michelotti, G. Roma, A. Belardini, N. Danz, A. Pace, F. Sarto, and R. M. Montoreali, "Micro-cavity organic light emitting diodes for biochip applications," *J. Non-Cryst. Solids*, vol. 352, nos. 23–25, pp. 2476–2479, 2006.

- [15] A. M. Adawi, L. G. Connolly, D. M. Whittaker, D. G. Lidzey, E. Smith, M. Roberts, F. Qureshi, C. Foden, and N. Athanassopoulou, "Improving the light extraction efficiency of red-emitting conjugated polymer light emitting diodes," *J. Appl. Phys.*, vol. 99, no. 5, p. 054505, 2006.
- [16] S.-H. Cho, Y.-W. Song, J. gu Lee, Y.-C. Kim, J. H. Lee, J. Ha, J.-S. Oh, S. Y. Lee, S. Y. Lee, K. H. Hwang, D.-S. Zang, and Y.-H. Lee, "Weak-microcavity organic light-emitting diodes with improved light out-coupling," *Opt. Express*, vol. 16, no. 17, pp. 12632–12639, 2008.
- [17] J.-S. Kim, P. K. H. Ho, N. C. Greenham, and R. H. Friend, "Electroluminescence emission pattern of organic light-emitting diodes: Implications for device efficiency calculations," *J. Appl. Phys.*, vol. 88, no. 2, pp. 1073–1081, 2000.
- [18] M.-H. Lu and J. C. Sturm, "Optimization of external coupling and light emission in organic light-emitting devices: Modeling and experiment," *J. Appl. Phys.*, vol. 91, no. 2, pp. 595–604, 2002.
- [19] L. H. Smith and W. L. Barnes, "Using a low-index host layer to increase emission from organic light-emitting diode structures," *Org. Electron.*, vol. 7, no. 6, pp. 490–494, 2006.
- [20] K. Celebi, T. D. Heidel, and M. A. Baldo, "Simplified calculation of dipole energy transport in a multilayer stack using dyadic green's functions," *Opt. Express*, vol. 15, no. 4, pp. 1762–1772, 2007.
- [21] S. P. Savaidis and N. A. Stathopoulos, "Simulation of light emission from planar multilayer OLEDs, using a transmission-line model," *IEEE J. Quantum Elect.*, vol. 45, no. 9, pp. 1089–1099, Sep. 2009.
- [22] K. B. Kahen, "Rigorous optical modeling of multilayer organic light-emitting diode devices," *Appl. Phys. Lett.*, vol. 78, no. 12, pp. 1649–1651, 2001.
- [23] V. Bulovic, V. B. Khalfin, G. Gu, P. E. Burrows, D. Z. Garbuzov, and S. R. Forrest, "Weak microcavity effects in organic light-emitting devices," *Phys. Rev. B*, vol. 58, no. 7, pp. 3730–3740, 1998.
- [24] J. M. Leger, S. A. Carter, B. Ruhstaller, H.-G. Nothofer, U. Scherf, H. Tillman, and H.-H. Hörhold, "Thickness-dependent changes in the optical properties of PPV- and PF-based polymer light emitting diodes," *Phys. Rev. B*, vol. 68, no. 5, p. 054209, 2003.
- [25] C. L. Mulder, K. Celebi, K. M. Milaninia, and M. A. Baldo, "Saturated and efficient blue phosphorescent organic light emitting devices with Lambertian angular emission," *Appl. Phys. Lett.*, vol. 90, no. 21, p. 211109, 2007.
- [26] T. Granlund, L. Pettersson, and O. Inganäs, "Determination of the emission zone in a single-layer polymer light-emitting diode through optical measurements," *J. Appl. Phys.*, vol. 89, no. 11, p. 5897, 2001.
- [27] B. Ruhstaller, S. A. Carter, S. Barth, H. Riel, W. Riess, and J. C. Scott, "Transient and steady-state behavior of space charges in multilayer organic light-emitting diodes," *J. Appl. Phys.*, vol. 89, no. 8, pp. 4575–4586, 2001.
- [28] B. Ruhstaller, T. Beierlein, H. Riel, S. Karg, J. Scott, and W. Riess, "Simulating electronic and optical processes in multilayer organic light-emitting devices," *IEEE J. Sel. Top. Quantum Electron.*, vol. 9, no. 3, pp. 723–731, May–Jun. 2003.
- [29] C. Pflumm, C. Gartner, and U. Lemmer, "A numerical scheme to model current and voltage excitation of organic light-emitting diodes," *IEEE J. Quantum Elect.*, vol. 44, no. 8, pp. 790–798, Aug. 2008.
- [30] N. Tessler, "Transport and optical modeling of organic light-emitting diodes," *Appl. Phys. Lett.*, vol. 77, no. 12, pp. 1897–1899, 2000.
- [31] K. Saxena, D. S. Mehta, R. Srivastava, and M. N. Kamalasanan, "Spatial coherence properties of electroluminescence from Alq3-based organic light emitting diodes," *Appl. Phys. Lett.*, vol. 89, no. 6, p. 061124, 2006.
- [32] D. Razansky, D. F. Soldea, and P. D. Einziger, "Bounds and estimates for power absorption in 2-D highly lossy configurations," *J. Appl. Phys.*, vol. 95, no. 12, pp. 8298–8308, 2004.
- [33] L. B. Felsen and N. Marcuvitz, *Radiation and Scattering of Waves*, 1st ed. Englewood Cliffs, NJ: Prentice-Hall, 1973.
- [34] P. D. Einziger, L. M. Livshitz, and J. Mizrahi, "Rigorous image-series expansions of quasi-static Green's functions for regions with planar stratification," *IEEE Trans. Antenn. Propag.*, vol. 50, no. 12, pp. 1813–1823, Dec. 2002.
- [35] A. Epstein, N. Tessler, and P. D. Einziger, "Electromagnetic radiation from organic light-emitting diodes," in *Proc. PIERS*, Beijing, China, 2009, pp. 1702–1707.
- [36] P. D. Einziger, L. M. Livshitz, and J. Mizrahi, *Biomathematics: Modeling and Simulation*. Singapore: World Scientific, 2006, ch. 12, pp. 315–358.
- [37] M. Born and E. Wolf, *Principles of Optics*. New York: Cambridge University Press, 1999.
- [38] A. Camposeo, L. Persano, P. D. Carro, D. G. Papazoglou, A. Stassinopoulos, D. Anglos, R. Cingolani, and D. Pisignano, "Longitudinal coherence of organic-based microcavity lasers," *Opt. Exp.*, vol. 16, no. 14, pp. 10384–10389, 2008.

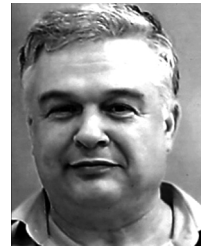
**Ariel Epstein** received the B.A. degree in computer science from the Open University of Israel, Raanana, Israel, and the B.A. degree in physics and the B.Sc. degree in electrical engineering from the Technion - Israel Institute of Technology, Haifa, Israel, in 2000 and 2003, respectively. He is currently working toward the Ph.D. degree from the Department of Electrical Engineering, Technion.

His current research interests include electromagnetic theory, nanoelectronic devices, and their common applications.



**Nir Tessler** received the B.Sc. (*summa cum laude*) in electrical engineering from Technion - Israel Institute of Technology, Haifa, Israel.

After "falling in love" with organic optoelectronics he strived to contribute to the understanding that organics can be used in numerous applications where the latest example was of polymer-based light-emitting diodes emitting at telecom wavelengths. In 1999, he joined the Technion as a Faculty Member studying new materials, device design and analysis, and charge transport and related phenomena in disordered amorphous materials-based devices.



**Pinchas D. Einziger** received the B.Sc. and M.Sc. degrees in electrical engineering from the Technion - Israel Institute of Technology, Haifa, Israel, and the Ph.D. degree in electrophysics from Polytechnic University, Brooklyn, NY, in 1976, 1978, and 1981, respectively.

Since 1981, he has been a Faculty Member with the Department of Electrical Engineering, Technion. His current research interests include electromagnetic wave theory, nonlinear wave phenomena, and bioelectromagnetics.